

Structural 3D Characterization of Silica Monoliths: Extraction of Rod Networks

Aaron Spettl¹, Mika Lindén², Ingo Manke³ and Volker Schmidt¹

¹ Ulm University, Institute of Stochastics,
Helmholtzstr. 18, D-89069 Ulm

² Ulm University, Institute of Inorganic Chemistry II,
Albert-Einstein-Allee 11, D-89081 Ulm

³ Helmholtz-Zentrum Berlin für Materialien und Energie, Institut für
Angewandte Materialforschung,
Hahn-Meitner-Platz 1, D-14109 Berlin

Abstract Based on experimental 3D image data, we analyze a highly porous silica monolith consisting of a network of rod-like structures. Because the rods are often hard to recognize even by visual inspection of the image data, a simple binarization with e.g. thresholding techniques is problematic. Therefore we extract a voxel-based skeleton directly from the filtered grayscale image, which is then transformed into vector data, i.e., a system of line segments describing the rod network. In a final step we complete the extraction by estimating a radius for every line segment, using the concept of the Hough transform applied to the gradient image. These steps yield a structural segmentation with advantages over global or local thresholding techniques and allow the statistical analysis and characterization of the given sample.

1 Introduction

Highly porous materials and the investigation of their complex pore architectures are important for many applications, e.g., drug delivery [1] and molecular separation by adsorption or chromatographic separation [2]. Besides the porosity, the connectivity of pores as well as the distributions of pore sizes and pore shapes are very important and not easily accessible. Using 3D imaging techniques the microstructure of porous materials

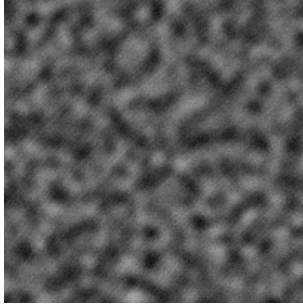


Figure 1.1: 2D cross-section of experimental image data, $60\mu\text{m} \times 60\mu\text{m}$

and, in particular, their pores can be analyzed, with the limitation to the spatial resolution implied by the chosen imaging technique. As an example of application, we investigate the 3D morphology of a silica monolith using synchrotron X-ray tomography, with a visible porosity of about 70%. The porosity including mesopores of the highly porous monolith is approximately 90%, but we only observe the macroporous morphology. Note that for pores on a smaller scale, different imaging techniques like FIB-SEM tomography may be necessary, where other problems occur in the segmentation process [3, 4].

The reconstructed grayscale image of our experimental data has a voxel size of $(215\text{ nm})^3$, see Figure 1.1 for a 2D cross-section. Visual inspection of the data suggests that a network of micrometer-sized rods might be suitable.

The algorithmic extraction of the network itself is performed by applying the λ -leveling operator proposed in [5], which has originally been designed for 2D images, but works analogously in 3D. The voxel-based skeleton is converted to a network given by vector data, which is achieved by detecting branches and representing their connections by line segments. The connecting line segments are approximated using the Douglas–Peucker algorithm [6, 7], which is an algorithm that reduces the number of points in a curve.

With the known locations of the rods, we use the idea of the Hough transform to detect a radius for every line segment based on the gradient image of the smoothed grayscale image [8, 9]. The rods themselves are

then given by the line segments and their corresponding radii.

Note that the segmentation result cannot be validated directly, because there is no reasonable reference segmentation. However, the quality of the algorithm can be justified by applying it to artificially generated test data with known structural properties.

2 Experimental Data and Preprocessing

2.1 Experimental Data

An exemplary silica monolith has been characterized by synchrotron X-ray tomography, the resulting grayscale image has a voxel size of $(215 \text{ nm})^3$, where a large homogeneous cut-out of $768 \times 768 \times 768$ voxels has been processed, see Figure 1.1 for a 2D cross-section. In the following, this observation window is denoted by $W = [0, 767] \times [0, 767] \times [0, 767]$.

While the total porosity of the material is approximately 90%, only the macropores are visible, which account for about 70% of the volume. The grayscale value of a voxel at position $(x, y, z) \in W$ in the considered grayscale image I is denoted by $I(x, y, z) \in [0, 255]$, where higher values indicate brighter regions, i.e., foreground.

2.2 Data Preprocessing

We applied a median filter with a box size of $3 \times 3 \times 3$ to remove noise and denote the filtered image by I' , i.e., $I'(x, y, z) = \text{median}(\{I(i, j, k), (i, j, k) \in W \cap [x-1, x+1] \times [y-1, y+1] \times [z-1, z+1]\})$.

A subsequent grayscale erosion using a ball with radius $\sqrt{2}$ as structuring element has the effect of highlighting the centers of the rods that we want to extract in the following. The result is denoted by I'' , i.e., $I''(x, y, z) = \min(\{I(i, j, k), (i, j, k) \in W \text{ with } \sqrt{(x-i)^2 + (y-j)^2 + (z-k)^2} \leq \sqrt{2}\})$.

Note that due to integer coordinates, this grayscale erosion is equivalent to a minimum-filtering in a 18-neighborhood in 3D. The effect of these filters is shown in Figure 1.2.

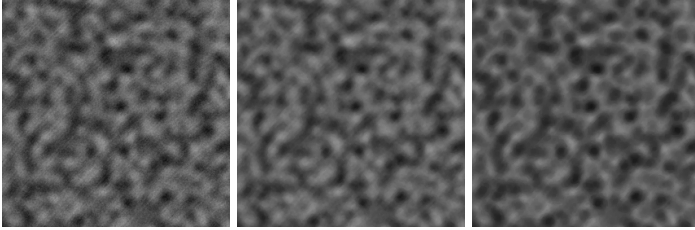


Figure 1.2: 2D cross-section of original image I (left), median-filtered image I' (center) and eroded image I'' (right)

3 Grayscale Skeletonization

The extraction of the rod network itself is performed by applying the λ -leveling operator proposed in [5], which has originally been designed for 2D images, but works analogously in 3D. The parameter λ is a non-negative integer that controls the tolerance against variations in grayscale values, i.e., too small values of λ cause an over-segmentation and too large values have the effect that structures are lost.

3.1 λ -Leveling and λ -Skeleton Operator

The idea of the λ -leveling operator is to lower the grayscale value of voxels without changing the topology in their neighborhood. These voxels are called λ -deletable, where λ is a local contrast parameter. The λ -leveling image is then obtained by iteratively choosing voxels whose grayscale value can be lowered and decreasing it to the lowest possible value, until stability is achieved. In 2D, the resulting image often consists of areas having constant grayscale values separated by lines with higher grayscale values. The λ -skeleton is naturally given by those lines, i.e., it consists of all voxels adjacent to at least one voxel with a smaller grayscale value. Note that by introducing the notion of λ -end points, we can avoid thinning of branches that would be iteratively removed otherwise. A detailed description including examples can be found in [5], e.g., how λ -deletable and λ -end points can be defined formally.

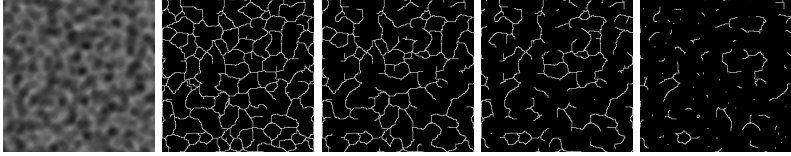


Figure 1.3: 2D input image (left) and 2D λ -skeleton for $\lambda = 20$, $\lambda = 40$, $\lambda = 60$ and $\lambda = 80$ (right)

3.2 Application to Experimental Data

For our data with grayscale values in $[0, 255]$, the parameter $\lambda = 60$ is a good choice, compare Figure 1.3 with examples of over- and under-segmentation. The parameter λ is chosen such that (in the 2D skeleton) only structures located clearly in the given 2D slice remain. Then, by computing the 3D skeleton, the skeleton voxels are automatically located in the correct slice.

We apply the skeleton operator to the eroded image I'' , because this image highlights the centers of rods and is therefore ideal for skeletonization. The resulting skeleton is a binary image S with $S(x, y, z) \in \{0, 255\}$. Note that λ -end points are preserved, because we do not want to lose rods having only one contact to the network. Figure 1.4 shows a 3D visualization of the voxel-based skeleton.

4 Extraction of Rod Network

The skeleton S obtained in the previous step is based on the voxel grid, but a network given by line segments is required. Those line segments define the start and end points of the rods, whose radii will be detected in a second step.

4.1 Network Extraction

The conversion of a voxel-based skeleton to a network of line segments is achieved by detecting branches and their connections. It is clear that all skeleton voxels having exactly two neighbors denote connections. Skeleton voxels with exactly one neighbor are end points, whereas skeleton

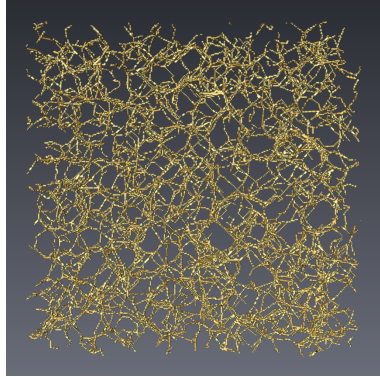


Figure 1.4: 3D visualization of the extracted skeleton (cut-out)

voxels with more than two neighbors are branching points. End points and branching points are therefore the vertices of the resulting network graph. Note that adjacent branching points are converted to a single vertex whose coordinates are given by their barycenter.

An edge connecting two vertices is represented by one or more line segments, depending on the tortuosity of the connection. The connection is given by voxels, i.e., their coordinates, which is a series of points. The Douglas–Peucker algorithm [6, 7] is an algorithm that reduces the number of points in a curve and is suitable to reduce the number of line segments, but upholding a given precision. The algorithm is often used in processing of vector graphics, e.g., rendering of maps. Given a series of points, it connects the start and end point, searches for the interior point with the maximal distance to this line segment, and replaces the segment by two segments if the distance is above a certain threshold. This is applied recursively until all original points are within a (small) distance to the set of extracted line segments.

4.2 Radii Detection for Rods

The axes including start and end points of the rods are exactly the extracted line segments. With the known location of the rods, we use the idea of the Hough transform (HT) [8]. The HT is a robust algorithm to

detect parameterized geometric objects. Generally, it suffers from high computing times, but in our case only one single parameter has to be determined.

The classical HT would require a binary image of detected edges of objects. To avoid binarization, we use the gradient image, as recently suggested in [9]. Instead of counting edge voxels covering the surface of a rod with the currently inspected radius, we sum up gradient values, which show the magnitude of changes in grayscale values. The gradient image of the smoothed grayscale image I' is given by $|\nabla I'(x, y, z)| = |(\frac{\partial}{\partial x} I'(x, y, z), \frac{\partial}{\partial y} I'(x, y, z), \frac{\partial}{\partial z} I'(x, y, z))|$. It is clear that for counting edge voxels or computing sums of gradient values, larger objects have a lot more potential for high values. To avoid over-estimation of object sizes, the values have to be rescaled. In [9], the factor $1/r^{\frac{1}{2}}$ has been suggested, which is also a good starting point for cylinders. However, for our experimental data, $1/r^{0.8}$ provides a better optical fit. This difference is probably caused by relatively wide areas with significant gradient magnitudes. For test data without this effect, the exponent 0.5 works very well.

Note that we have to restrict the gradient image to the relevant parts for each rod. This is important because otherwise the gradient values caused by other (adjacent) rods could have an influence on the detection of the currently processed rod. This is implemented by applying the watershed algorithm [10, 11] to the inverted smoothed grayscale image $255 - I'(\cdot)$. The result is a partition of the window W into basins B_1, \dots, B_n , where bright areas of the original image are in the center of basins and so-called watersheds correspond to borders between brighter regions. The complete relevant region for a single rod is then given by all basins intersecting with the currently processed line segment.

4.3 Results

Recall that the rods themselves are now given by the line segments and the detected radii, as described above. The result of the extraction looks quite promising, compare Figures 1.5 and 1.6. Objects clearly visible are detected, their dimensions seem plausible and the general structure is not lost. Therefore, the porosity of the extracted data is also as anticipated: it is about 0.66, where approximately 0.7 is expected.

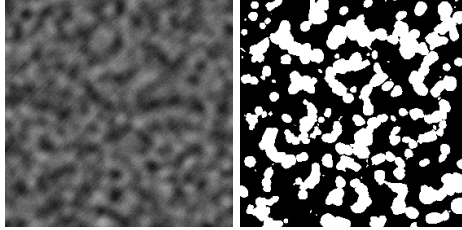


Figure 1.5: 2D cross-section of experimental image data (left) and extracted rod network (right)

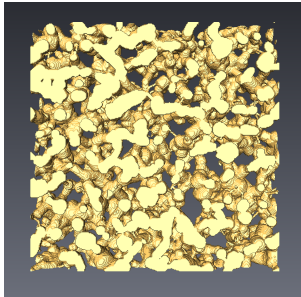


Figure 1.6: 3D visualization of a thin cut-out of extracted rod network

5 Validation

The segmentation result derived in Sections 3 and 4 cannot be validated directly, because there is no reasonable reference segmentation. However, the quality of the algorithm can be justified by applying it to artificially generated test data with known structural properties.

A very simple example based on a cube-shaped network illustrates the procedure, compare Figure 1.7. Note that the vertices are slightly shifted, which is caused by the skeletonization algorithm. Nevertheless, the resulting extracted rods reproduce the input image very well. In the following, we will look at a random rod network and compare its structural characteristics.

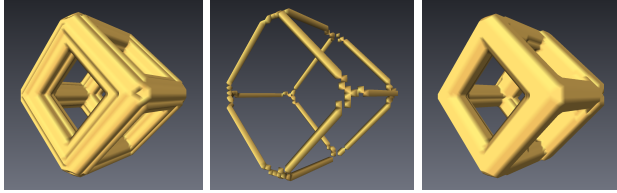


Figure 1.7: Simple example in 3D: cube-shaped network (left), extracted skeleton (center), extracted rod network (right)

5.1 Test Data

Artificial test data of mutually overlapping cylinders has been generated by realizing a random geometric graph, including random radii for all line segments and plotting all resulting cylinders into a binary image. Furthermore, the binary image has been blurred and noise has been added, see Figure 1.8.

We use a simple stochastic model for the random geometric graph, with numeric marks for all edges. The vertices of the graph are given by a random point process that enforces a minimum distance between points, i.e., it is a Matérn hard-core point process [12]. Then, for the two nearest neighbors of every vertex, an edge is generated with a certain probability p , in our case $p = 0.8$. Finally, the marks for all edges are modeled by independent Gamma-distributed random variables.

5.2 Extraction of Rod Network

The rod network has been extracted as described in Section 4, with preprocessing and skeletonization as in Sections 2 and 3.

5.3 Results

While the optical fit is not perfect, see Figures 1.8 and 1.9, the general structure is clearly represented. By looking closely it can be suspected that radii are often overestimated, especially in the case of overlapping rods. This is not surprising, because the Hough transform cannot differentiate between edges caused by the considered rod and another overlapping rod. The histogram of rod radii supports this theory: there is a

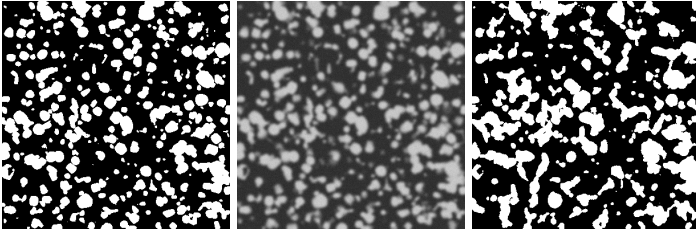


Figure 1.8: Exemplary 2D cross-section of artificial test data (left), blurred and noisy test data (center), and extracted rod network (right)

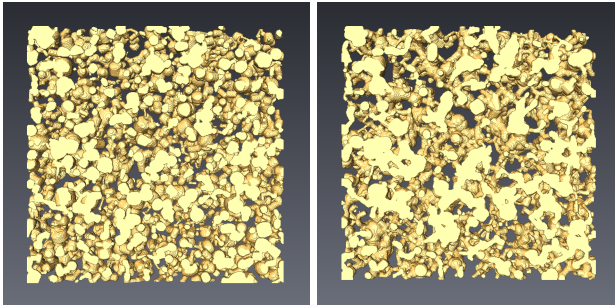


Figure 1.9: 3D visualization of a thin cut-out of artificial test data (left) and extracted rod network (right)

clear tendency towards larger radii, compare Figure 1.10. Nevertheless, the histograms of coordination numbers, i.e., the numbers of edges per vertex of the network graph, are nearly the same, compare Figure 1.11.

6 Summary and Conclusion

In this paper, we have introduced a technique suitable to extract rod networks from 3D grayscale images, based on the combination of several well-known algorithms. Binarization of the 3D image is avoided in all steps. After smoothing of experimental image data, we extract a 3D skeleton using a grayscale skeletonization, which takes one parameter to

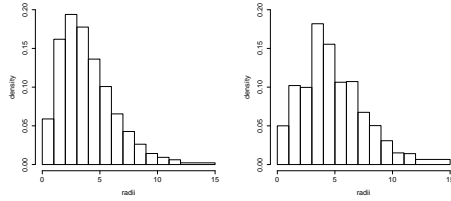


Figure 1.10: Histogram of radii of artificial test data (left) and extracted rod network (right)

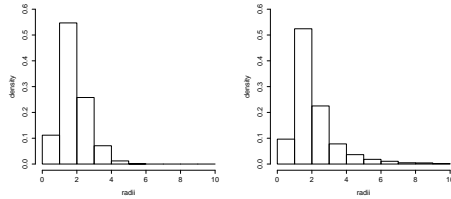


Figure 1.11: Histogram of coordination number of artificial test data (left) and extracted rod network (right)

control the local contrast necessary for skeleton voxels to appear. After conversion from skeleton voxels to a network of line segments, only the radii of the rods have to be detected. The Hough transform is used to detect the missing object parameter, but it is applied to the gradient image instead of a binary image of object edges.

While it is not known whether this type of silica monolith consists exclusively of rods, the segmentation describes the grayscale image very well and obtained characteristics like porosity are as expected. The proposed algorithm has been validated using artificial test data. A perfect fit is not achieved, but this is clearly not a realistic goal – information is lost by blurring the image, but in particular, overlapping rods are a problem for every technique trying to detect the optimal radii or even positions of rods.

References

1. K. Khanafer and K. Vafai, “The role of porous media in biomedical engineering as related to magnetic resonance imaging and drug delivery,” *Heat and Mass Transfer*, vol. 42, pp. 939–953, 2006.
2. F. Dullien, *Porous Media, Fluid Transport, and Pore Structure*, 2nd ed. New York: Academic Press Inc., 1992.
3. M. Salzer, A. Spettl, O. Stenzel, J. Smätt, M. Lindén, I. Manke, and V. Schmidt, “A two-stage approach to the segmentation of FIB-SEM images of highly porous materials,” *Materials Characterization*, vol. 69, pp. 115–126, 2012.
4. M. Salzer, S. Thiele, R. Zengerle, and V. Schmidt, “On automatic segmentation of FIB-SEM images,” in *Forum Bildverarbeitung 2012*, F. Puente León and M. Heizmann, Eds. Karlsruhe: KIT Scientific Publishing, 2012, to appear.
5. M. Couprie, F. Bezerra, and G. Bertrand, “Topological operators for grayscale image processing,” *Journal of Electronic Imaging*, vol. 10, p. 1003, 2001.
6. D. Douglas and T. Peucker, “Algorithms for the reduction of the number of points required to represent a digitized line or its caricature,” *The Canadian Cartographer*, vol. 10, pp. 112–122, 1973.
7. U. Ramer, “An iterative procedure for the polygonal approximation of plane curves,” *Computer Graphics and Image Processing*, vol. 1, pp. 244–256, 1972.
8. D. Ballard, “Generalizing the Hough transform to detect arbitrary shapes,” *Pattern Recognition*, vol. 13, no. 2, pp. 111–122, 1981.
9. R. Thiedmann, A. Spettl, O. Stenzel, T. Zeibig, J. Hindson, Z. Saghi, N. Greenham, P. Midgley, and V. Schmidt, “Networks of nanoparticles in organic–inorganic composites: algorithmic extraction and statistical analysis,” *Image Analysis and Stereology*, vol. 31, no. 1, pp. 27–42, 2012.
10. R. Beare and G. Lehmann, “The watershed transform in ITK - discussion and new developments,” *The Insight Journal*, June 2006.
11. J. Roerdink and A. Meijster, “The watershed transform: definitions, algorithms, and parallelization strategies,” *Fundamenta Informaticae*, vol. 41, pp. 187–228, 2000.
12. J. Illian, A. Penttinen, H. Stoyan, and D. Stoyan, *Statistical Analysis and Modelling of Spatial Point Patterns*. Chichester: J. Wiley & Sons, 2008.